

Gravitational axial perturbations of Schwarzschild-like black holes in dark matter halos

Chao Zhang^{a,b,c,*}, Tao Zhu^{a,b,†} and Anzhong Wang^{d,‡}

^a *Institute for Theoretical Physics and Cosmology,
Zhejiang University of Technology, Hangzhou, 310032, China*

^b *United Center for Gravitational Wave Physics (UCGWP),
Zhejiang University of Technology, Hangzhou, 310032, China*

^c *College of Information Engineering, Zhejiang University of Technology, Hangzhou, 310032, China*

^d *GCAP-CASPER, Physics Department, Baylor University, Waco, Texas 76798-7316, USA*

(Dated: February 10, 2022)

Gravitational waves emitted by distorted black holes, such as those arising from the coalescence of binary black holes, or a falling compact star into a supermassive black hole, carry not only information about the corresponding spacetime but also the information about the environment surrounding the black holes. In this paper, we study the effects of the dark matter halos with three different density profiles on the gravitational axial perturbations of a Schwarzschild-like black hole. For this purpose, we first consider modified Schwarzschild black holes with three different dark matter profiles and derive the equation of motion of the axial perturbations of the modified Schwarzschild metric. It is shown that by ignoring the dark matter perturbations, a Regge-Wheeler-like master equation with a modified potential for the axial perturbation can be obtained explicitly. Then we calculate the complex frequencies of the quasinormal modes of the Schwarzschild-like black hole in the dark matter halos by applying the sixth-order WKB method. The corresponding gravitational wave spectra with the effects of the dark matter halos have also been discussed.

I. INTRODUCTION

Black holes (BHs) are one of the most mysterious phenomena in the Universe. The existence of BHs provides us a perfect way to test gravitational effects under extremely strong gravity, such as the formation of gigantic jets of particles and disruption of neighboring stars [1]. On the other hand, from the theoretical point of view, BHs are also unique labs to test modified theories of gravity that are different from general relativity (GR) (see, e.g., [2–4]).

The outbreak of interest on BHs has further gained momenta after the detection of the shadow of the M87 central BH with the Event Horizon Telescope (EHT) [5–12]. In fact, it is widely believed that the central region of many galaxies contain supermassive BHs. The shadow image of the M87 central BH captured by EHT is in good agreement with the prediction of the spacetime geometry of a BH described by the Kerr metric [13]. Nonetheless, since it is believed that up to 90% of the matter in a host galaxy is made up by dark matter (DM) [14], it is natural to expect that the DM halo surrounding a central BH will bring small deviations to the Kerr metric.

Although DM has not been directly detected, many evidences imply its existence. In addition, because of the rotation curves of galaxies, the mass-light ratio of elliptical galaxies, the cosmic microwave background radiation, and the large-scale structure of the cosmos, a lot of research has been done on DM and proposed various DM

models [15]. Of course, there are many open questions related to DM, for instance, the spatial density distribution of DM in galaxies, solutions of Einstein’s field equations when considering the DM background, and more.

In this paper, we focus on the effects of DM halos on gravitational waves (GWs) emitted from the central BH located in a galaxy. The detection of the first GW from the coalescence of two massive BHs by advanced LIGO marked the beginning of a new era, the GW astronomy [16]. Following this observation, about 90 GW events have been identified by the LIGO/Virgo/KAGRA scientific collaborations (see, e.g., [17–20]). In the future, more ground- and space-based GW detectors will be constructed [21–24], which will enable us to probe signals with a wider frequency band. This triggered the interests on the quasinormal modes (QNMs) from GWs, including those from the late-merger and ringdown stages of coalescence [25] as well as those from supermassive BHs, e.g., central BHs in a galaxy. The detection of QNMs from the ringdown stage will provide a unique way to probe the matter environment surrounding a BH. For example, it is shown that the shift from GR on the QNMs due to the surrounding ultralight bosons might be detectable in the future by the observational data from LISA-like missions [26]. The effects of the dark matter or matter distributing around BHs on the QNMs have also been considered in [27–29].

From the theoretical point of view, QNMs are eigenmodes of dissipative systems. The information contained in QNMs provide the keys for revealing whether BHs are ubiquitous in our Universe, and more important whether GR is the correct theory to describe the event even in the strong field regime. Readers may find more details in [30]. Basically, the QNM frequency ω contains two parts,

* chao123@zjut.edu.cn

† corresponding author: zhut05@zjut.edu.cn

‡ anzhong.wang@baylor.edu

the real part and the imaginary part. Its real part gives the frequency of vibration while its imaginary part provides the damping time. In other words, the frequency we are going to calculate is a complex number (although it could be purely imaginary in certain circumstances).

In fact, in GR according to the no-hair theorem, an isolated BH is completely characterized by only three quantities, mass, spin angular momentum and electric charge. Astrophysically, we expect BHs to be neutral, so they ought to be described by the Kerr solution. Then, the quasinormal frequencies and damping times will depend only on the mass and angular momentum of a BH. Therefore, to extract the physics from QNMs, at least two QNM signals are needed. This will require the signal-to-noise ratio (SNR) to be of the order 100. Although such high SNRs are not achievable right now, it has been shown that they may be achievable once the advanced LIGO and Virgo reach their designed sensitivities. In any case, it is certain that they will be detected by the ground-based third-generation detectors, such as Cosmic Explorer or the Einstein Telescope, as well as the space-based detectors, including LISA, TianQin [32], Taiji [24], and DECIGO [21].

For this purpose, we first consider modified Schwarzschild black holes with three different DM profiles and derive the equation of motion of the axial perturbations¹ of the modified Schwarzschild metric. It is shown that by ignoring the DM perturbations, a Regge-Wheeler (RW)-like master equation with a modified potential for the axial perturbation can be obtained explicitly. Then we calculate the frequencies of the QNMs of the Schwarzschild-like black hole in the DM halos by applying the sixth-order WKB method. The corresponding GW spectra with the effects of the DM halos have also been discussed.

Here, we consider the QNMs of the axial metric perturbations of a Schwarzschild-like BH surrounded by the DM halos. Several different background metrics are investigated by considering three different DM profiles. These metrics for different dark matter halo profiles can be found in [1, 34]. Note that recently the metric of a black hole immersed in dark matter spike has also been derived [31]. In addition, the Sgr A* black hole (located in the center of Milky Way Galaxy) and the M87 galactic central black hole are what we focus on. In other words, the structure we consider is a BH located at the center of a galaxy. By comparing the resultant ω 's with their counterparts for the Schwarzschild case, we see the influence of

DM halo on QNMs as well as GWs from central BHs. At the same time, we will also estimate the detectability of these deviations from the Schwarzschild case. Finally, by varying some profile-dependent constants, one can find out how these ω 's are deviating from the Schwarzschild case with the effects of the DM halos.

The rest of this paper is organized as follows. Sec. II shows some basic information of the three density profiles of DM halos that we investigate for the calculations of QNMs. After that, in Sec. III we show how to derive a Regge-Wheeler-like master equation from the axial perturbation and Einstein's field equations. At the same time, we show a brief analysis of the effective potentials under different DM profiles (including that from the Schwarzschild case). Section IV contains two parts. In the first part, we present some resultant ω 's. Some concluding remarks are given by comparing them with their counterparts in the Schwarzschild case. For the second part, we test the effects of model-dependent constants. Some results are shown together with an analysis. Finally, Sec. V provides our main conclusions as well as some outlooks for future work.

Through out the paper, we adopt the unit system so that $c = G_N = 1$, where c is the speed of light, while G_N stands for the gravitational constant observed on Earth. In this way, we still have one degree of freedom to choose the unit for length. This is done later by setting $r_{\text{MH}} = 1$, where r_{MH} means the radius of the metric horizon (MH) of the BH that we are focusing on. In this paper, all the greek indices run from 0 to 3. Other usage of indices is indicated explicitly when it is necessary.

II. BLACK HOLE SOLUTIONS IN DARK MATTER HALO

Normally, the black hole spacetimes are not clean and are affected by the surrounding matters. In this section, we consider the spherically symmetric static black hole solutions with several different DM halo profiles. In general, a Schwarzschild BH in the DM halo is described by the metric [34]

$$ds^2 = -G(r)dt^2 + \frac{1}{G(r)}dr^2 + r^2d\theta^2 + r^2\sin^2\theta d\varphi^2, \quad (2.1)$$

where $G(r)$ denotes the function that describes the effects of the DM halos and BH on the metric and it reduces to the Schwarzschild solution, viz., $G(r) = 1 - 2M/r$ [35], when the DM is absent. For different profiles of the DM halo, the function $G(r)$ is different [34]. In the following, we present the function $G(r)$ for each profile individually.

A. URC profile

In the universal rotation curve (URC) profile of the DM halo, the distribution of the DM is described by [36]

¹ Normally, the GW spectrum of QNMs can be studied via black hole perturbations. In the background spacetime which is static and spherically symmetric, the metric perturbations can decouple into two independent parts, the polar one and the axial one. In this paper we only consider the latter case. As we discuss later, the axial perturbation considered in this paper is equivalent to the odd-parity perturbation, which corresponds to the parity of $(-1)^l$, with l being an index inherited from spherical harmonics [33].

(see also [37] for a review)

$$\rho(r) = \frac{\rho_0 r_0^3}{(r + r_0)(r^2 + r_0^2)}, \quad (2.2)$$

where ρ_0 is the central density and r_0 is the characteristic radius of the DM halo. According to the observations on the M87 galaxy, the best fit values for the parameters of the URC profile are $\rho_0 = 6.9 \times 10^6 \text{M}_\odot/\text{kpc}^3$ and $r_0 = 91.2 \text{ kpc}$ [38]. While in the Milky Way Galaxy, we have $\rho_0 = 5.2 \times 10^7 \text{M}_\odot/\text{kpc}^3$ and $r_0 = 7.8 \text{ kpc}$ [39]. With this halo profile, the function $G(r)$ in the metric (2.1) is given by [1, 40]

$$\begin{aligned} G(r) = & e^{-2\pi^2 \rho_0 r_0^2} \left(1 + \frac{r^2}{r_0^2} \right)^{-\frac{2\rho_0 r_0^3 \pi}{r} (1 - \frac{r}{r_0})} \\ & \times \left(1 + \frac{r}{r_0} \right)^{-\frac{4\rho_0 r_0^3 \pi}{r} (1 + \frac{r}{r_0})} \\ & \times \exp \left[\frac{4\rho_0 r_0^3 \pi \arctan(\frac{r}{r_0})(1 + \frac{r}{r_0})}{r} \right] - \frac{2M}{r}. \end{aligned} \quad (2.3)$$

Here $M = 6.5 \times 10^9 \text{ M}_\odot$ for the M87 central BH and $M = 4.3 \times 10^6 \text{ M}_\odot$ for the Sgr A* BH.

B. The CDM halo with NFW profile

The cold dark matter (CDM) halo with a Navarro-Frenk-White (NFW) profile is obtained by N -body simulations, which has a universal spherically averaged density profile [1, 41]

$$\rho(r) = \frac{\rho_0}{(r/r_0)(1 + r/r_0)^2}, \quad (2.4)$$

where ρ_0 is the density of the Universe at the moment when the halo collapsed and r_0 is the characteristic radius. According to the observations on the Milky Way Galaxy [39], the best fit values for the parameters ρ_0 and r_0 for the NFW profile are $\rho_0 = 5.23 \times 10^7 \text{M}_\odot/\text{kpc}^3$ and $r_0 = 8.1 \text{ kpc}$. On the other hand, for the M87 galaxy, we have $\rho_0 = 0.008 \times 10^{7.5} \text{ M}_\odot/\text{kpc}^3$ (see [42]) and $r_0 = 130 \text{ kpc}$ [1]. With this halo profile, the function $G(r)$ in the metric (2.1) is given by [34]

$$G(r) = \left(1 + \frac{r}{r_0} \right)^{-\frac{8\pi G_N \rho_0 r_0^3}{c^2 r}} - \frac{2G_N M}{c^2 r}. \quad (2.5)$$

Here $M = 4.3 \times 10^6 \text{ M}_\odot$ is the mass of Sgr A* BH, and $M = 6.5 \times 10^9 \text{ M}_\odot$ is the mass of M87 central BH.

C. The SFDM model

For the scalar field dark matter (SFDM) model [43], the energy density profile for a DM halo is given by

$$\rho(r) = \frac{\rho_0 \sin(\pi r/r_0)}{\pi r/r_0}, \quad (2.6)$$

where ρ_0 is the central density and r_0 is the radius at which the pressure and density are zero. In the Milky Way Galaxy, we have $\rho_0 = 3.43 \times 10^7 \text{M}_\odot/\text{kpc}^3$ and $r_0 = 15.7 \text{ kpc}$ [43]. With this halo profile, the function $G(r)$ in the metric (2.1) is given by

$$G(r) = \exp \left[-\frac{8G_N \rho_0 R^2}{\pi} \frac{\sin(\pi r/r_0)}{\pi r/r_0} \right] - \frac{2G_N M}{c^2 r}. \quad (2.7)$$

Here $M = 4.3 \times 10^6 \text{ M}_\odot$ is the mass of Sgr A* BH.

III. REGGE-WHEELER-LIKE EQUATION FOR AXIAL METRIC PERTURBATIONS

In this section, we consider the linear gravitational perturbations $h_{\mu\nu}$ around Schwarzschild-like solutions. Let us first start with a general form of a spherically symmetric spacetime, given by [44]

$$ds^2 = -G(r)dt^2 + F^{-1}(r)dr^2 + H(r)d\Omega^2, \quad (3.1)$$

where

$$d\Omega^2 = d\theta^2 + \sin^2 \theta d\phi^2. \quad (3.2)$$

Of course, for our case [cf. (2.1)], we have $G = F$ and $H = r^2$. For metric perturbations, let us start by describing the geometry of a linearly perturbed spherically symmetric background $\bar{g}_{\mu\nu}$

$$g_{\mu\nu} = \bar{g}_{\mu\nu} + h_{\mu\nu}, \quad (3.3)$$

where

$$\bar{g}_{\mu\nu} = \text{diag} \left(-G(r), \frac{1}{F(r)}, H(r), H(r) \sin^2 \theta \right), \quad (3.4)$$

where $h_{\mu\nu}$ denotes the linear perturbations of the background metric $\bar{g}_{\mu\nu}$. In general, the perturbation $h_{\mu\nu}$ can be split into pieces that transform as scalars, vectors, and tensors with respect to the symmetry of the spacetime. However, in two-dimensional maximally symmetric space S^2 , it can be shown that the tensor perturbations with transverse-traceless conditions are identically zero [45–47]. Thus, the metric perturbations can be split as scalar and vector perturbations, i.e., $h_{\mu\nu} = h_{\mu\nu}^S + h_{\mu\nu}^V$. Here, we note that the scalar perturbation is also called a polar-type perturbation (or even-parity perturbation), while the vector one is called an axial perturbation (or odd-parity perturbation) [30]. In this paper, for simplicity, we only focus on the axial perturbations of the Schwarzschild-like solutions with different dark matter halos.

We parametrize the axial perturbations in the form of [48]

$$h_{\mu\nu} = \sum_{l=0}^{\infty} \sum_{m=-l}^l \begin{pmatrix} 0 & 0 & -C_{lm} \csc \theta \partial_{\varphi} & C_{lm} \sin \theta \partial_{\theta} \\ 0 & 0 & -J_{lm} \csc \theta \partial_{\varphi} & J_{lm} \sin \theta \partial_{\theta} \\ \text{sym} & \text{sym} & -W_{lm} \csc \theta (\cot \theta \partial_{\varphi} - \partial_{\theta} \partial_{\varphi}) & \text{sym} \\ \text{sym} & \text{sym} & \frac{1}{2} W_{lm} (\csc \theta \partial_{\varphi}^2 + \cos \theta \partial_{\theta} - \sin \theta \partial_{\theta}^2) & W_{lm} (\cos \theta \partial_{\theta} - \sin \theta \partial_{\theta} \partial_{\varphi}) \end{pmatrix} Y_{lm}(\theta, \varphi) \epsilon, \quad (3.5)$$

where C_{lm} , J_{lm} , and W_{lm} are functions of t and r . The $Y_{lm}(\theta, \varphi)$ stands for the spherical harmonics [49], and the l as well as m in the index are integers. Here, ϵ is a real number, and $|\epsilon| \ll 1$.

From now on, we set $m = 0$ in (3.5) so that $\partial_{\varphi} Y_{lm}(\theta, \varphi) = 0$. As of now, the background has the spherical symmetry, and the corresponding linear perturbations do not depend on m [48, 50]. In addition, by adopting the RW gauge [48], we set $W_{lm} = 0$.

The Einstein equations are given by

$$E_{\mu\nu} \equiv R_{\mu\nu} - \frac{1}{2} R g_{\mu\nu} = 8\pi G_N T_{\mu\nu}, \quad (3.6)$$

where $R_{\mu\nu}$ and R are the Ricci tensor and Ricci scalar, respectively [35], and $T_{\mu\nu}$ denotes the energy-momentum tensor due to the presence of DM. For simplicity, here, we ignore the perturbation of the DM since its effects are expected to be negligible in comparing to the effects of DM from the modified background geometry. Then, expanding E_{23} and E_{13} to leading order of ϵ , we obtain

$$0 = -\frac{\dot{C}}{G} + \frac{(GF' + FG')}{2G} J + FJ', \quad (3.7)$$

$$0 = \frac{H'}{H} \dot{C} - \dot{C}' + \ddot{J} + \frac{1}{2} \left[F'G' + \frac{G \left\{ H [F'H' + 2(FH'' + l^2 + l - 2)] - F(H')^2 \right\}}{H^2} - \frac{F(G')^2}{G} + F \left(2G'' + \frac{G'H'}{H} \right) \right] J, \quad (3.8)$$

where a dot stands for the time derivative, while a prime stands for the derivative with respects to r . Notice that we have dropped the lm in the subscripts of C and J for simplicity. After that, by combining (3.7) and (3.8), we obtain the master equation

$$\frac{d^2 \Psi(t, x)}{dx^2} - \left[\frac{d^2}{dt^2} + V_{\text{eff}}(r) \right] \Psi(t, x) = 0, \quad (3.9)$$

where

$$\Psi \equiv \left(\frac{H}{GF} \right)^{-1/2} J, \quad (3.10)$$

$$\frac{dr}{dx} = \sqrt{FG}, \quad (3.11)$$

and the effective potential is given by

$$V_{\text{eff}} \equiv \frac{1}{4} \left[2F'G' + \frac{G \left\{ H [F'H' + 2FH'' + 4(l^2 + l - 2)] + F(H')^2 \right\}}{H^2} - \frac{2F(G')^2}{G} + F \left(4G'' + \frac{G'H'}{H} \right) \right]. \quad (3.12)$$

By assuming $\Psi = e^{-i\omega t} \Psi(x)$, Eq. (3.9) could be written as

$$\frac{d^2 \Psi(x)}{dx^2} + [\omega^2 - V_{\text{eff}}(r)] \Psi(x) = 0. \quad (3.13)$$

Following Sec. II, we list the cases that we consider for the calculations of QNMs in Table I and provide some basic information for each case. They are referred to as case 1, 2 and 3, respectively. Note that the master equations and QNMs for case 2 and case 3 have also been

studied in [28] with relatively larger values of r_0 and ρ_0 . The Schwarzschild case is also shown.

To find the difference between different cases, the V_{eff} 's for each case listed in Table I are plotted in Fig. 1. To make them at the same starting line, the data for the Milky Way are selected for plotting. In addition, as an example, we have set $l = 2$ for this plot. Notice that, as noted earlier, here we are using the unit system so that $c = G_N = r_{\text{MH}} = 1$. From Fig. 1, it is very clear that

TABLE I. Summary of the cases that we consider for the calculations of QNMs.

Case	Galaxy	$G(r)$	ρ_0 (M_\odot/kpc^3)	r_0 (kpc)
Schwarzschild	N/A	$1 - \frac{2M}{r}$	0	N/A
Case 1	M87	(2.3)	6.9×10^6	91.2
	Milky Way	(2.3)	5.2×10^7	7.8
Case 2	M87	(2.5)	$0.008 \times 10^{7.5}$	130
	Milky Way	(2.5)	5.23×10^7	8.1
Case 3	Milky Way	(2.7)	3.43×10^7	15.7

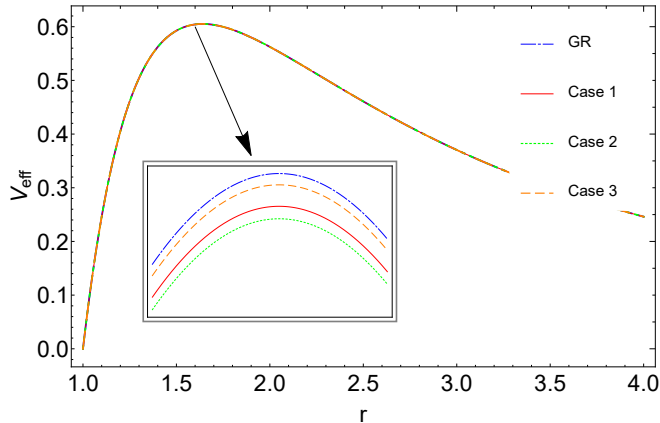


FIG. 1. Behaviors of V_{eff} for different cases listed in Table I, in which the data for the Milky Way is selected for plotting. In addition, we have chosen $l = 2$. Note that there is an inserted figure showing the amplification of the region around the stationary points of these curves. Also note that here we are using the unit system so that $c = G_N = r_{\text{MH}} = 1$.

the deviation on V_{eff} 's between each two cases in Table I is quite small since these curves are almost overlapped. Actually, it is because of this, that an amplification of the region around the stationary points of these curves of V_{eff} 's is inserted, so that readers can find more details. That implies we may obtain quite similar QNMs from these cases in the end. As we see, this is indeed the case.

IV. QNMS OF SCHWARZSCHILD-LIKE BLACK HOLE IN DM HALOS

With the master equation given by (3.13), we are ready to solve for the corresponding ω , viz., the QNM, for a specific set of $\{G, F, H\}$, including the cases listed in Table I (as well as their extensions by varying ρ_0 or r_0). Note that the QNMs for cases 2 and 3 have also been considered in [28] with larger values of ρ_0 and ρ_0 . Notice that, ω , in general, is a complex number, often written as ω_{lmn} [30], where l and m are inherited from spherical harmonics while n is the overtone index. However, since we have set $m = 0$, it is left with two indices only, i.e., l and n (For simplicity, before stimulating any confusions,

we write ω_{ln} as ω).

Once again, for all the cases mentioned above, we adopt the unit system so that $c = G_N = r_{\text{MH}} = 1$. Here, the radius of the MH is given by $r_{\text{MH}} = (2G_N M)/c^2$ [35]. In this way, the units for mass, time, and length are totally fixed.

A. Calculations of QNMs for the cases in Table I

So far, we have obtained the desired master equation [cf. (3.13)], and we have several background metrics (see Table I). In addition, we also know the two boundary conditions, namely, the pure in-going wave at the MH and pure out-going wave at the spatial infinity [51]. With everything in hand, and given a set of $\{l, n\}$, we can find the corresponding ω_{ln} , in principle.

QNMs in GR with the Schwarzschild case have been studied extensively. In this procedure, several different techniques of calculations were developed, for instance, the Wentzel-Kramers-Brillouin (WKB) approach [52–55], the continued fraction method [56], shooting method [51], etc.[57–59]. After scrutinizing these methods, we noticed that the WKB method is probably the most convenient way for our current problem. Therefore, we use the sixth-order WKB method to carry out our calculations.

The formula of ω from the sixth-order WKB method is given by

$$\omega = \sqrt{-i \left[\left(n + \frac{1}{2} \right) + \sum_{k=2}^6 \Lambda_k \right] \sqrt{-2V_0''} + V_0}, \quad (4.1)$$

where

$$V_0 \equiv V_{\text{eff}}|_{r=r_{\text{max}}}, \quad V_0'' \equiv \left. \frac{dV_{\text{eff}}}{dr^2} \right|_{r=r_{\text{max}}}, \quad (4.2)$$

with $V_{\text{eff}}(r = r_{\text{max}})$ giving the maximum of V_{eff} on $r \in (1, \infty)$. The expressions of Λ_k 's can be found in [52–54]. Note that $n = 0, 1, 2, \dots$

In this subsection, we adopt the choices given by Table I to carry out the calculations. The results of ω 's for this part are exhibited in Tables II - IV for case 1, 2 and 3, respectively. Note that in these tables, the results for BHs with DM halos are compared with their

TABLE II. The QNMs ω 's that calculated from the sixth-order WKB method for BHs with DM halos by adopting the background and factors given in case 1 of Table I. Note that each ω here is compared to its Schwarzschild counterpart.

l	n	M87	Milky Way	ω 's of BHs in Schwarzschild case
2	0	$0.74718 - 0.17776i$	$0.74724 - 0.17778i$	$0.74724 - 0.17778i$
	1	$0.69254 - 0.54690i$	$0.69259 - 0.54696i$	$0.69259 - 0.54696i$
	2	$0.59700 - 0.95502i$	$0.59704 - 0.95511i$	$0.59704 - 0.95512i$
3	0	$1.19879 - 0.18539i$	$1.19888 - 0.18540i$	$1.19889 - 0.18541i$
	1	$1.16519 - 0.56252i$	$1.16528 - 0.56258i$	$1.16528 - 0.56258i$
	2	$1.10310 - 0.95799i$	$1.10318 - 0.95809i$	$1.10319 - 0.95809i$
4	0	$1.61823 - 0.18831i$	$1.61835 - 0.18833i$	$1.61836 - 0.18833i$
	1	$1.59313 - 0.56861i$	$1.59326 - 0.56866i$	$1.59326 - 0.56867i$
	2	$1.54527 - 0.95970i$	$1.54538 - 0.95979i$	$1.54539 - 0.95980i$

TABLE III. The QNMs ω 's that calculated from the sixth-order WKB method for BHs with DM halos by adopting the background and factors given in case 2 of Table I. Note that each ω here is compared to its Schwarzschild counterpart.

l	n	M87	Milky Way	ω 's of BHs in Schwarzschild case
2	0	$0.74723 - 0.17778i$	$0.74723 - 0.17778i$	$0.74724 - 0.17778i$
	1	$0.69259 - 0.54695i$	$0.69259 - 0.54696i$	$0.69259 - 0.54696i$
	2	$0.59704 - 0.95511i$	$0.59704 - 0.95511i$	$0.59704 - 0.95512i$
3	0	$1.19888 - 0.18540i$	$1.19888 - 0.18540i$	$1.19889 - 0.18541i$
	1	$1.16528 - 0.56258i$	$1.16528 - 0.56258i$	$1.16528 - 0.56258i$
	2	$1.10318 - 0.95808i$	$1.10318 - 0.95809i$	$1.10319 - 0.95809i$
4	0	$1.61834 - 0.18833i$	$1.61835 - 0.18833i$	$1.61836 - 0.18833i$
	1	$1.59325 - 0.56866i$	$1.59325 - 0.56866i$	$1.59326 - 0.56867i$
	2	$1.54538 - 0.95979i$	$1.54538 - 0.95979i$	$1.54539 - 0.95980i$

Schwarzschild counterparts. It should be mentioned here that during the calculations for case 1, since (2.3) is quite complicated and will arise technical difficulties when performing derivatives, the V_{eff} for case 1 is expanded before processing to (4.1). In other words, we use the polynomial form of V_{eff} in case 1. To be more specific, we expand it as

$$V_{\text{eff}} = \sum_{k=0}^{99} \beta_k \left(r - \frac{79}{50} \right)^k. \quad (4.3)$$

In this way, we have $\left| V_{\text{eff}}|_{\text{original}} - V_{\text{eff}}|_{\text{polynomial}} \right| \lesssim \mathcal{O}(10^{-19})$ on $r \in (r_{\text{MH}}, r_{\text{max}})$ for $l = 2, 3, 4$, and thus, the accuracy of QNMs is guaranteed.

By looking at Tables II - IV, we immediately notice that the deviations between the Schwarzschild and non-Schwarzschild cases occur at the fourth digit or after that. For most of the ω 's in Tables II - IV, these deviations are very small, just like we anticipated earlier. Considering the fact that our calculations contain numerical errors, these deviations are quite negligible. Nonetheless, we can also observe a relatively large deviation on, e.g., ω_{40} of case 1 for the M87 galaxy, which could probably meet the designed resolution of the TianQin detector (cf. Table II of [32]). That means, according to the current results, we may be able to obtain more constraints for the URC profile by using the observational data from TianQin-like detectors in the future.

B. Tests of the impacts of ρ_0 and r_0 on QNMs

In the above subsection, we have considered the impacts of DM halos on QNMs by adopting the halo parameters ρ_0 and r_0 given in Table I. It is worth mentioning here that these parameters are, in general, derived by fitting the corresponding density profiles with the observational data of the rotation curves in different galaxies, see [39] for examples. Thus, these profiles roughly reflect DM distributions for the whole galaxy. They tend to be accurate in describing the regions far away from the central BH. In contrast, to the contexts of the matter environment around the central BH, the halo parameters ρ_0 and r_0 are basically free. Moreover, in the central region around a BH, the baryonic component also makes significant contributions to the halo parameters.

In addition, the values of ρ_0 and r_0 also change from galaxy to galaxy. In the Milky Way, $r_0 \sim 10$ kpc and $\rho_0 \sim 10^7 M_{\odot}/\text{kpc}^3$, as presented in Table I. Depending on specific galaxies, it is shown that in the catalog of dark matter halo models for galaxies in the Spitzer Photometry and Accurate Rotation Curves (SPARC) database r_0 can be as large as ~ 700 kpc, and ρ_0 can be as large as $10^{10} M_{\odot}/\text{kpc}^3$ for a NFW profile [60]. In the SPARC, 175 galaxies are included. Thus, it is natural to expect that the values of ρ_0 or r_0 in some galaxies in the Universe could be even larger than those given in SPARC.

For these three reasons, it is worth investigating how the frequencies of QNMs shift with freely changing ρ_0 and r_0 in different profiles. We do the calculations based on Table I. Nevertheless, this time we try different values

TABLE IV. The QNMs ω 's that calculated from the sixth-order WKB method for BHs with DM halos by adopting the background and factors given in case 3 of Table I. Note that each ω here is compared to its Schwarzschild counterpart.

l	n	M87	Milky Way	ω 's of BHs in Schwarzschild case
2	0	N/A	$0.74724 - 0.17778i$	$0.74724 - 0.17778i$
	1	N/A	$0.69259 - 0.54696i$	$0.69259 - 0.54696i$
	2	N/A	$0.59704 - 0.95512i$	$0.59704 - 0.95512i$
3	0	N/A	$1.19888 - 0.18540i$	$1.19889 - 0.18541i$
	1	N/A	$1.16528 - 0.56258i$	$1.16528 - 0.56258i$
	2	N/A	$1.10319 - 0.95809i$	$1.10319 - 0.95809i$
4	0	N/A	$1.61835 - 0.18833i$	$1.61836 - 0.18833i$
	1	N/A	$1.59326 - 0.56867i$	$1.59326 - 0.56867i$
	2	N/A	$1.54539 - 0.95980i$	$1.54539 - 0.95980i$

of ρ_0 and r_0 in addition to those appearing in Table I. Of course, the procedures of calculating QNMs for this part are quite similar to those in the last subsection.

First of all, in Fig. 2, we plot the results of ω_{20} , ω_{30} , and ω_{40} by changing the values of ρ_0 as well as r_0 in case 1 (cf. Table I). In panels (a) and (b), the r_0 is fixed to be 7.8 kpc, while in panels (c) and (d) the ρ_0 is fixed to be $5.2 \times 10^7 M_\odot/\text{kpc}^3$. From panels (a) and (b), we observe that both $\text{Re}(\omega)$ and $\text{Im}(\omega)$ are very close to their limits of the Schwarzschild case (cf., e.g., Table II) at the beginning when $\rho_0 \approx 10^6 M_\odot/\text{kpc}^3$. However, these ω 's will soon deviate from the Schwarzschild case when ρ_0 is approaching $\rho_0 \approx 10^{12} M_\odot/\text{kpc}^3$. Similarly, from panel (c) and (d), we observe that both $\text{Re}(\omega)$ and $\text{Im}(\omega)$ are very close to their limits of the Schwarzschild case at the beginning when $r_0 \approx 1\text{kpc}$. However, these ω 's will soon deviate from the Schwarzschild case when r_0 is approaching $r_0 \approx 2500\text{kpc}$.

After that, by mimicking Fig. 2, we plot the results of ω_{20} , ω_{30} , and ω_{40} by changing the values of ρ_0 as well as r_0 for case 2 and 3 (cf. Table I) in Figs. 3 and 4, respectively. Basically, we could see quite similar behaviors of ω 's in these two figures, just like what we have seen in Fig. 2. Therefore, we do not carry out further analysis to these cases.

From Figs. 2, 3, and 4, it is easy to observe that the QNM frequency is changing as ρ_0 or r_0 increasing. When r_0 is fixed, the real part of the QNM frequency is decreasing, while the imaginary part is increasing as ρ_0 increases. Similar behaviors also appear when one fixes ρ_0 and increases r_0 . When ρ_0 and r_0 become larger, the density of DM becomes bigger accordingly. These features indicate that the real part of QNM frequency becomes lower, while the imaginary part becomes larger for a denser DM distribution around the BH.

In order to see how the above shifts on QNM frequencies affect the GWs from the ringdown stages of coalescences, we need to construct the corresponding GW waveform. The GW emitted during the ringdown stage can be expressed as a linear combination of damped sinusoids

$$h_+ + ih_\times = \frac{M_z}{D_L} \sum_{lmn} \mathcal{A}_{lmn} e^{i(f_{lmn}t + \phi_{lmn})} e^{-t/\tau_{lmn}} S_{lmn},$$

where M_z is the redshifted mass of the black hole, D_L the luminosity distance to the source, \mathcal{A}_{lmn} the mode amplitude, ϕ_{lmn} the phase coefficient, and S_{lmn} the (complex) spin-weighted spheroidal harmonics of spin weight 2, which depend on the polar and azimuthal angles. The GW frequency $f_{lmn} = \text{Re}(\omega_{lmn})$ is the real part of the QNM frequency for (l, m, n) mode, while the damping time τ_{lmn} is related to the imaginary part of the QNM frequency via $\tau_{lmn} = -1/\text{Im}(\omega_{lmn})$. From the above waveform, it is evident that a denser DM distribution in the central region near a BH leads to lower GW frequency and longer damping time for GWs during the ringdown stage. Considering the designed resolution of space-based detectors, such as LISA, TianQin, and Taiji, these effects may be detectable. This may provide an approach to probe the matter distribution in the central region of a galaxy.

V. CONCLUSION AND OUTLOOKS

In this paper, we study the calculations of QNMs for spherically symmetric BHs [cf. (2.1)] with DM halos. We are caring about how DM halos influence the QNMs and thus the GWs from a central BH located in a galaxy. Several different DM profiles are investigated for the M87 galaxy as well as the Milky Way Galaxy, which are referred as case 1, 2, and 3, respectively (cf. Table I). In addition, we have focused on the axial perturbation on the background spacetimes, which are parametrized by (3.5).

The backgrounds we consider are described by Eqs. (2.3), (2.5), and (2.7) for these three different cases. From their expressions we observe that the effects of DM halos are determined by two factors, viz., r_0 and ρ_0 . By using Einstein's field equations [cf. (3.6)] with a general spherically symmetric background metric [cf. (3.1)], a Regge-Wheeler-like master equation is obtained [cf. (3.13)], for which the RW gauge is adopted [48]. With this in hand, and provided a specific set of $\{l, n\}$ (recall that we have set $m = 0$), we are able to calculate the corresponding QNMs.

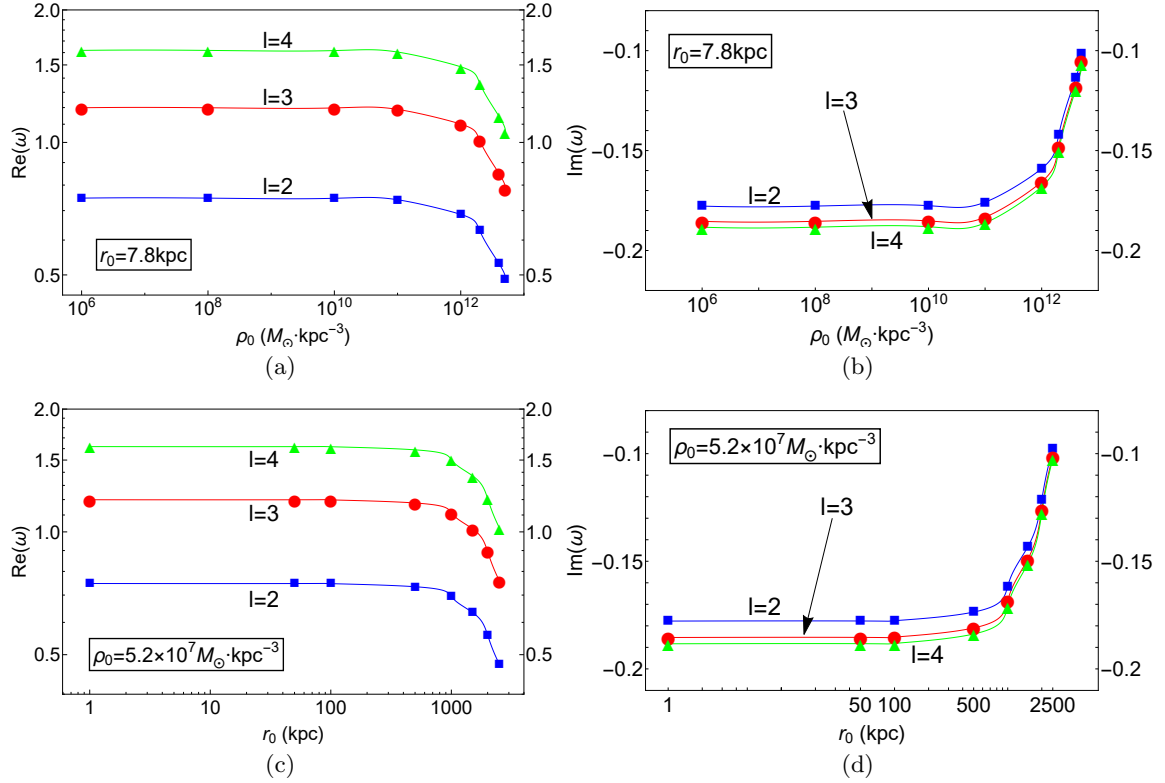


FIG. 2. Results of ω_{20} , ω_{30} , and ω_{40} by changing the values of ρ_0 as well as r_0 in case 1 (cf. Table I). Panels (a) and (c) show $\text{Re}(\omega)$, while panels (b) and (d) show $\text{Im}(\omega)$. Note that in panels (a) and (b) r_0 is fixed to be 7.8 kpc, while in panels (c) and (d) ρ_0 is fixed to be $5.2 \times 10^7 M_\odot/\text{kpc}^3$. Also note that for the above ω 's we are adopting the unit system so that $c = G_N = r_{\text{MH}} = 1$.

According to the experience with GR, there are many different methods for the calculations of QNMs. Nonetheless, in practice, we noticed that the most convenient way for our problem is the WKB method. Therefore, the sixth-order WKB method [cf. (4.1)] is used here for calculating QNMs. The results of ω 's are exhibited in Tables II - IV for case 1, 2, and 3 (cf. Table I), respectively. Note that, in there we have selected the unit system so that $c = G_N = r_{\text{MH}} = 1$.

For most of the ω 's in Tables II - IV, we notice that the deviations between the Schwarzschild and non-Schwarzschild cases are quite small. Considering the fact that our calculations contain numerical errors, these deviations are quite negligible. Nonetheless, we can also observe a relatively large deviation, which occurs at the fourth digit, e.g., ω_{40} of case 1 for the M87 galaxy. It is worth mentioning here that such a discrepancy could be within the designed resolution of space-based GW detectors, such as LISA, TianQin, and Taiji [32]. Once they are in operation in the future, one may obtain more constraints for the URC profile by matching the observational data with the results of QNMs in here. More importantly, this result implies the possibility of confining DM profiles with GW observations in the future.

Since the values of ρ_0 and r_0 may change from galaxy to galaxy, we also investigate the impacts of them on

QNMs. Indeed, according to the current observations to the Milky Way Galaxy and M87 galaxy, the resultant ρ_0 and r_0 will lead to quite negligible deviations from the Schwarzschild case (cf., e.g., Fig. 1). Nonetheless, it is hard to tell what kind of parameters we will obtain for other galaxies in the Universe. Thus, it is worth checking what will happen when ρ_0 and r_0 are changing freely. More importantly, in the context of constraints on BH environments, these parameters are basically free [27]. It is not necessary to assume that they will preserve similar magnitudes in all the occasions. A more reasonable way is to consider ρ_0 and r_0 on a wider range. This fact stimulates our interests on how these parameters will influence the QNMs when they are changing freely.

Basically, we study the influence of one of the two parameters ρ_0 and r_0 on QNMs by fixing the other. The corresponding results are shown in Figs. 2-4. From these figures, it is very clear that the resultant ω 's will approach their limits in the Schwarzschild case when ρ_0 and r_0 are getting smaller. In contrast, we can see significant deviations on ω 's from the Schwarzschild case for sufficiently large ρ_0 and r_0 . In addition, we observe that these deviations have been large enough so that we cannot solely attribute them to numerical errors. For an arbitrary galaxy in the Universe, it is possible to have large enough ρ_0 and r_0 since they are essentially known

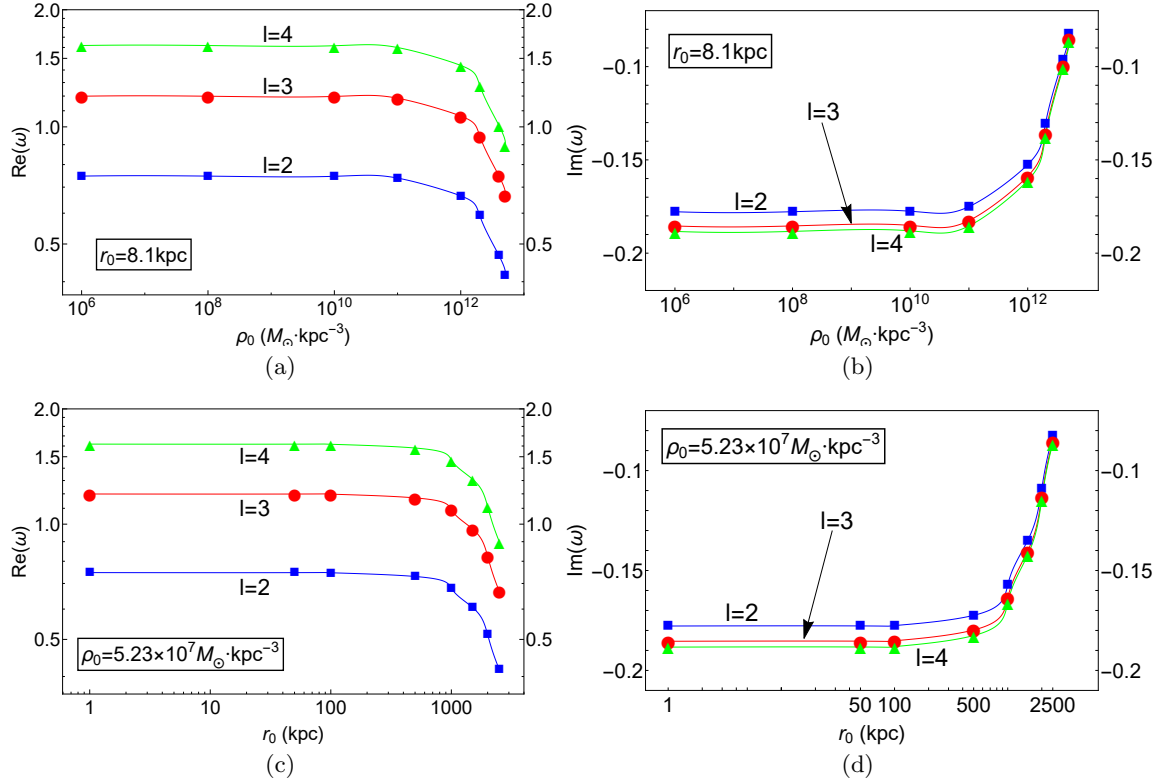


FIG. 3. Results of ω_{20} , ω_{30} , and ω_{40} by changing the values of ρ_0 as well as r_0 in case 2 (cf. Table I). Panels (a) and (c) show $\text{Re}(\omega)$, while panels (b) and (d) show $\text{Im}(\omega)$. Note that in panels (a) and (b) r_0 is fixed to be 8.1 kpc, while in panels (c) and (d) ρ_0 is fixed to be $5.23 \times 10^7 M_\odot/\text{kpc}^3$. Also note that for the above ω 's we are adopting the unit system so that $c = G_N = r_{\text{MH}} = 1$.

to be free parameters. Therefore, according to the results here, a big deviation on QNMs between the Schwarzschild and non-Schwarzschild cases will occur. It is shown that the real part of QNM frequencies becomes smaller while the imaginary part becomes larger for denser DM distribution in the central region around a BH. This implies that the larger dark matter density in the central region near a BH leads to a lower GW frequency and longer damping time for GWs during the ringdown stage. Finally, by considering the designed resolution of LISA-like detectors, one may expect such a large deviation to be found in reality once a galaxy with suitable ρ_0 and r_0 is observed someday. By matching with the results here, these kinds of observations will either confirm our current understanding to DM or help us put constraints on the current DM models.

Our work here can be extended in several directions. First of all, here, we only consider three different DM profiles. It is interesting to extend the current work to other DM profiles, for instance, BHs surrounded by su-

perfluid DM and baryonic matter [14]. On the other hand, since astrophysical BHs, in general, have nonzero angular momentum, it is also our plan to extend our work to rotating BHs. In addition, the even-parity perturbations could also be investigated. Finally, we may test the effects of DM halos on various modified theories of gravity.

ACKNOWLEDGEMENTS

This work is supported by the National Key Research and Development Program of China Grant No. 2020YFC2201503, the Zhejiang Provincial Natural Science Foundation of China under Grants No. LR21A050001 and No. LY20A050002, the National Natural Science Foundation of China under Grants No. 11675143 and No. 11975203, and the Fundamental Research Funds for the Provincial Universities of Zhejiang in China under Grant No. RF-A2019015.

[1] K. Jusufi, M. Jamil, P. Salucci, T. Zhu, and S. Haroon, Black hole surrounded by a dark matter halo in the

M87 galactic center and its identification with shadow images, Phys. Rev. D **100**, 044012 (2019).

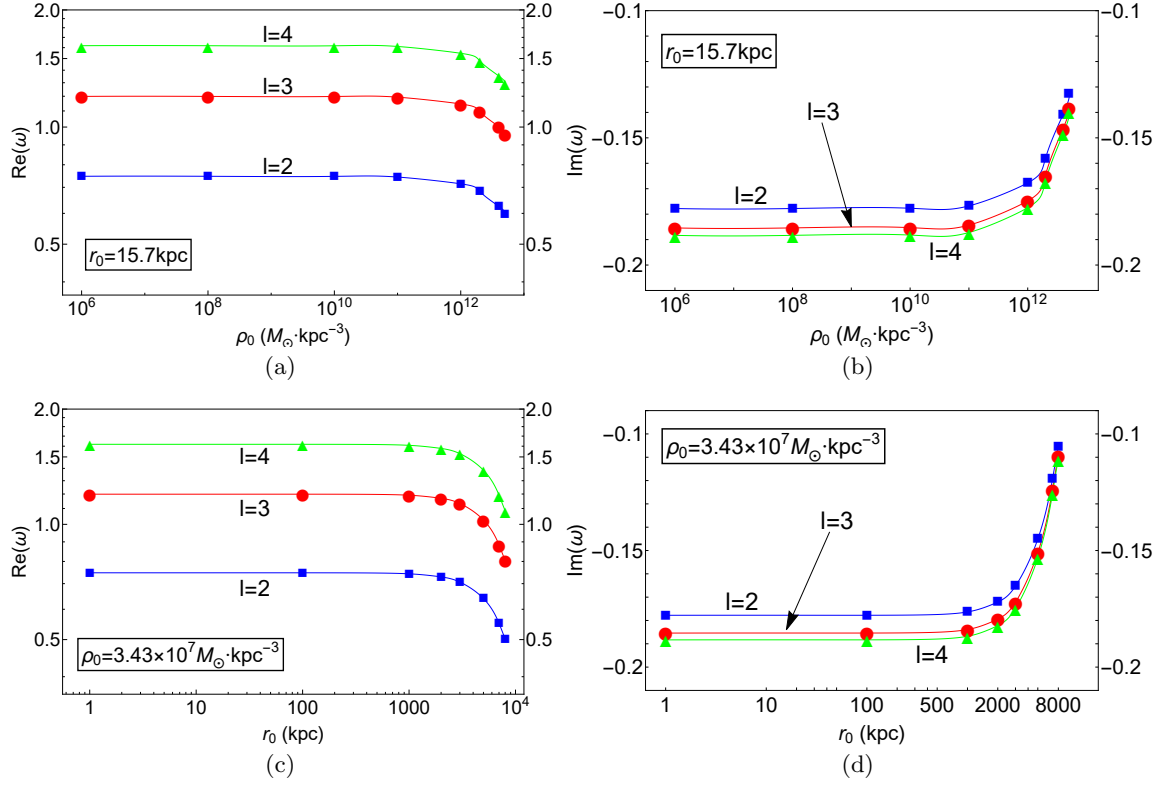


FIG. 4. Results of ω_{20} , ω_{30} and ω_{40} by changing the values of ρ_0 as well as r_0 in Case 3 (cf. Table I). Panel (a) and (c) show $\text{Re}(\omega)$ while Panel (b) and (d) show $\text{Im}(\omega)$. Note that in Panel (a) and (b) r_0 is fixed to be 8.1kpc, while in Panel (c) and (d) ρ_0 is fixed to be $3.43 \times 10^7 M_\odot / \text{kpc}^3$. Also note that for the above ω 's we are adopting the unit system so that $c = G_N = r_{\text{MH}} = 1$.

- [2] X. Zhao, C. Zhang, K. Lin, T. Liu, R. Niu, B. Wang, S.-J. Zhang, X. Zhang, W. Zhao, T. Zhu, and A. Wang, Gravitational waveforms and radiation powers of the triple system PSR J0337+1715 in modified theories of gravity, *Phys. Rev. D* **100**, 083012 (2019).
- [3] C. Zhang, X. Zhao, A. Wang, B. Wang, K. Yagi, N. Yunes, W. Zhao, and T. Zhu, Gravitational waves from the quasicircular inspiral of compact binaries in Einstein-aether theory, *Phys. Rev. D* **101**, 044002 (2020).
- [4] C. Zhang, X. Zhao, K. Lin, S.-J. Zhang, W. Zhao, and A.-Z. Wang, Spherically symmetric static black holes in Einstein-aether theory, *Phys. Rev. D* **102**, 064043 (2020).
- [5] K. Akiyama *et al.* (Event Horizon Telescope Collaboration), First M87 Event Horizon Telescope results. I. The shadow of the supermassive black hole, *Astrophys. J.* **875**, L1 (2019).
- [6] K. Akiyama *et al.* (Event Horizon Telescope Collaboration), First M87 Event Horizon Telescope results. II. Array and instrumentation, *Astrophys. J.* **875**, L2 (2019).
- [7] K. Akiyama *et al.* (Event Horizon Telescope Collaboration), First M87 Event Horizon Telescope results. III. Data processing and calibration, *Astrophys. J.* **875**, L3 (2019).
- [8] K. Akiyama *et al.* (Event Horizon Telescope Collaboration), First M87 Event Horizon Telescope results. IV. Imaging the central supermassive black hole, *Astrophys. J.* **875**, L4 (2019).
- [9] K. Akiyama *et al.* (Event Horizon Telescope Collaboration), First M87 Event Horizon Telescope results. V. Physical origin of the asymmetric ring, *Astrophys. J.* **875**, L5 (2019).
- [10] K. Akiyama *et al.* (Event Horizon Telescope Collaboration), First M87 Event Horizon Telescope results. VI. The shadow and mass of the central black hole, *Astrophys. J.* **875**, L6 (2019).
- [11] K. Akiyama *et al.* (Event Horizon Telescope Collaboration), First M87 Event Horizon Telescope results. VII. Polarization of the ring, *Astrophys. J.* **910**, L12 (2021).
- [12] K. Akiyama *et al.* (Event Horizon Telescope Collaboration), First M87 Event Horizon Telescope results. VIII. Magnetic field structure near The Event Horizon, *Astrophys. J.* **910**, L13 (2021).
- [13] R. P. Kerr, Gravitational Field of a Spinning Mass as an Example of Algebraically Special Metrics, *Phys. Rev. Lett.* **11**, 237 (1963).
- [14] K. Jusufi, M. Jamil, and T. Zhu, Shadows of Sgr A* black hole surrounded by superfluid dark matter halo, *Eur. Phys. J. C* **80**, 354 (2020).
- [15] Z. Xu, X. Gong, and S. Zhang, Black hole immersed dark matter halo, *Phys. Rev. D* **101**, 024029 (2020).
- [16] B.P. Abbott, *et al.*, [LIGO/Virgo Scientific Collaborations], Observation of Gravitational Waves from a Binary Black Hole Merger, *Phys. Rev. Lett.* **116**, 061102 (2016).
- [17] B.P. Abbott *et al.* (LIGO/Virgo Collaborations), GWTC-1: A Gravitational-Wave Transient Catalog of Compact Binary Mergers Observed by LIGO and Virgo during the First and Second Observing Runs, *Phys. Rev. X* **9**, 031040 (2019).

- [18] B.P. Abbott *et al.* (LIGO/Virgo Collaborations), Open data from the first and second observing runs of Advanced LIGO and Advanced Virgo, *SoftwareX* **13**, 100658 (2021).
- [19] B.P. Abbott *et al.* (LIGO/Virgo Collaborations), GW190425: Observation of a compact binary coalescence with total mass $\sim 3.4M_{\odot}$, *Astrophys. J. Lett.* **892**, L3 (2020).
- [20] B.P. Abbott *et al.* (LIGO/Virgo/KAGRA Collaborations), GWTC-3: Compact binary coalescences observed by LIGO and Virgo during the second part of the third observing run, arXiv:2111.03606v1.
- [21] C. J. Moore, R. H. Cole, and C. P. L. Berry, Gravitational-wave sensitivity curves, *Classical Quantum Gravity* **32**, 015014 (2015).
- [22] Y. Aso, Y. Michimura *et al.*, Interferometer design of the KAGRA gravitational wave detector, *Phys. Rev. D* **88**, 043007 (2013).
- [23] S. Liu, Y. Hu *et al.*, Science with the TianQin observatory: Preliminary results on stellar-mass binary black holes, *Phys. Rev. D* **101**, 103027 (2020).
- [24] W.-H. Ruan, Z.-K. Guo, R.-G. Cai, and Y.-Z. Zhang, Taiji program: Gravitational-wave sources, *Int. J. Mod. Phys. A* **35**, 2050075 (2020).
- [25] E. Berti, K. Yagi, H. Yang, and N. Yunes, Extreme gravity tests with gravitational waves from compact binary coalescences: (II) ringdown, *Gen. Relativ. Gravit.* **50**, 49 (2018).
- [26] A. K. W. Chung, J. Gais, M. H. Y. Cheung, and T. G. F. Li, Searching for ultralight bosons with supermassive black hole ringdown, *Phys. Rev. D* **104**, 084028 (2021).
- [27] V. Cardoso, K. Destounis, F. Duque, R. P. Macedo, and A. Maselli, (F)hairy tails: black holes in galaxies, [arXiv:2109.00005 [gr-qc]].
- [28] D. Liu, Y. Yang, S. Wu, Y. Xing, Z. Xu, and Z. W. Long, Ringing of a black hole in a dark matter halo, *Phys. Rev. D* **104**, 104042 (2021).
- [29] R. A. Konoplya, Black holes in galactic centers: Quasinormal ringing, grey-body factors and Unruh temperature, *Phys. Lett. B* **823**, 136734 (2021).
- [30] E. Berti, V. Cardoso, and A. O. Starinets, Quasinormal modes of black holes and black branes, *Classical Quantum Gravity* **26**, 163001 (2009).
- [31] Z. Xu and J. Wang, Deformed black hole immersed in dark matter spike, *J. Cosmol. Astropart. Phys.* **09** (2021) 007.
- [32] C.-F. Shi *et al.*, Science with the TianQin observatory: Preliminary results on testing the no-hair theorem with ringdown signals, *Phys. Rev. D* **100**, 044036 (2019).
- [33] V. Cardoso and J. P. S. Lemos, Quasinormal modes of Schwarzschild-anti-de Sitter black holes: Electromagnetic and gravitational perturbations, *Phys. Rev. D* **64**, 084017 (2001).
- [34] Z. Xu, X. Hou, X. Gong, and J. Wang, Black Hole Space-Time in Dark Matter Halo, *J. Cosmol. Astropart. Phys.* **09** (2018) 038.
- [35] S. Carroll, *Spacetime and Geometry-An Introduction to General Relativity* (Pearson Education Inc., Glenview, IL, 60025, USA, 2004).
- [36] P. Salucci and A. Burkert, Dark matter scaling relations, *Astrophysical J.* **537**, L9 (2000).
- [37] P. Salucci, The distribution of dark matter in galaxies, *Astron. Astrophys. Rev.* **27**, 2 (2019).
- [38] F. Donato, G. Gentile, P. Salucci, C. Frigerio Martins, M. Wilkinson, G. Gilmore, E. Grebel, A. Koch, and R. Wyse, A constant dark matter halo surface density in galaxies, *Mon. Not. R. Astron. Soc.* **397**, 1169 (2009).
- [39] H.-N. Lin and X. Li, The dark matter profiles in the Milky Way, *Mon. Not. R. Astron. Soc.* **487**, 5679 (2019).
- [40] S. Haroon, M. Jamil, K. Jusufi, K. Lin, and R. B. Mann, Shadow and deflection angle of rotating black holes in perfect fluid dark matter with a cosmological constant, *Phys. Rev. D* **99**, 044015 (2019).
- [41] J. F. Navarro, C. S. Frenk, S. D. M. White, A universal density profile from hierarchical clustering, *Astrophysical J.* **490**, 493 (1997).
- [42] L. J. Oldham and M. W. Auger, Galaxy structure from multiple tracers – II. M87 from parsec to megaparsec scales, *Mon. Not. R. Astron. Soc.* **457**, 421 (2016).
- [43] X. Hou, Z. Xu, M. Zhou, and J. Wang, Black hole shadow of Sgr A* in dark matter halo, *J. Cosmol. Astropart. Phys.* **07** (2018) 015.
- [44] M. B. Cruz, C. A. S. Silva, and F. A. Brito, Gravitational axial perturbations and quasinormal modes of loop quantum black holes, *Eur. Phys. J. C* **79**, 157 (2019).
- [45] R.-G. Cai and L.-M. Cao, Generalized formalism in gauge-invariant gravitational perturbations, *Phys. Rev. D* **88**, 084047 (2013).
- [46] T. Takahashi and J. Soda, Hawking radiation from fluctuating black holes, *Class. Quantum Grav.* **27**, 175008 (2010).
- [47] T. Takahashi and J. Soda, Master equations for gravitational perturbations of static Lovelock black holes in higher dimensions, *Prog. Theor. Phys.* **124**, 911-24 (2010).
- [48] J. E. Thompson, H. Chen, and B. F. Whiting, Gauge invariant perturbations of the Schwarzschild spacetime, *Classical Quantum Gravity* **34**, 174001 (2017).
- [49] N. Zettili, *Quantum Mechanics: Concepts and Applications* (2nd ed.) (CPI Antony Rowe Ltd, Chippenham, Wiltshire, UK, 2009).
- [50] T. Regge and J. A. Wheeler, Stability of a schwarzschild singularity, *Phys. Rev.* **108**, 4 (1957).
- [51] S. Chandrasekhar, F. R. S., and S. Detweiler, The quasinormal modes of the Schwarzschild black hole, *Proc. R. Soc. A.* **344**, 411 (1975).
- [52] B. F. Schutz and C. M. Will, Black hole normal modes: A semianalytic approach, *Astrophys. J.* **291**, L33 (1985).
- [53] S. Iyer and C. M. Will, Black-hole normal modes: A WKB approach. I. Foundations and application of a higher-order WKB analysis of potential-barrier scattering, *Phys. Rev. D* **35**, 12 (1987).
- [54] R. A. Konoplya, Quasinormal behavior of the D-dimensional Schwarzschild black hole and the higher order WKB approach, *Phys. Rev. D* **68**, 024018 (2003).
- [55] J. Matyjasek and M. Opala, Quasinormal modes of black holes: The improved semianalytic approach, *Phys. Rev. D* **96**, 024011 (2017).
- [56] E. W. Leaver, An analytic representation for the quasinormal modes of Kerr black holes, *Proc. R. Soc. A.* **402**, 285 (1985).
- [57] R. A. Konoplya and A. Zhidenko, Quasinormal modes of black holes: From astrophysics to string theory, *Rev. Mod. Phys.* **83**, 793 (2011).
- [58] C. Gundlach, R. H. Price, and J. Pullin, Late-time behavior of stellar collapse and explosions. I. Linearized perturbations, *Phys. Rev. D* **49**, 883 (1994).

- [59] B. Wang, C.-Y. Lin, and C. Molina, Quasinormal behavior of massless scalar field perturbation in Reissner-Nordström anti-de Sitter spacetimes, *Phys. Rev. D* **70**, 064025 (2004).
- [60] P. Li, F. Lelli, S. McGaugh, and J. Schombert, A comprehensive catalog of dark matter halo models for SPARC galaxies, *Astrophys. J. Suppl.* **247**, 31 (2020); see also <http://astroweb.cwru.edu/SPARC/>